Chinese Society of Aeronautics and Astronautics
& Beihang University

Chinese Journal of Aeronautics

cja@buaa.edu.cn
www.sciencedirect.com

FULL LENGTH ARTICLE

Rotor cross-tilt optimization for yaw control improvement of multi-rotor eVTOL aircraft

Xufei YAN [a], Ye YUAN [b], Yanqin ZHAO [c], Renliang CHEN [c],*

[a] *Zhejiang Lab, Hangzhou 311100, China*
[b] *Department of Aerospace Engineering, Swansea University, Swansea, Wales SA2 8PP, UK*
[c] *National Key Laboratory of Rotorcraft Aeromechanics, Nanjing University of Aeronautics and Astronautics, Nanjing 210016, China*

Abstract Manned multi-rotor electric Vertical Takeoff and Landing (eVTOL) aircraft is prone to actuator saturation due to its weak yaw control efficiency. To address this inherent problem, a rotor cross-tilt configuration is applied in this paper, with an optimization method proposed to improve the overall control efficiency of the vehicle. First, a flight dynamics model of a 500-kg manned multi-rotor eVTOL aircraft is established. The accuracy of the co-axial rotor model is verified using a single arm test bench, and the accuracy of the flight dynamics model is verified by the flight test data. Then, an optimization method is designed based on the flight dynamics model to calculate an optimal rotor cross-tilt mounting angle, which not only improves the yaw control efficiency, but also basically maintains the efficiency of other control channels. The ideal rotor cross-tilt mounting angle for the prototype is determined by comprehensively considering the optimal results with different payloads, forward flight speeds, and rotor mounting angle errors. Finally, the feasibility of the rotor cross-tilt mounting angle is proved by analyzing the control derivatives of the flight dynamics model, the test data of a ground three Degree-of-Freedom (3DOF) platform, and the actual flight data of the prototype. The results show that a fixed rotor cross-tilt mounting angle can achieve ideal yaw control effectiveness, improving yaw angle tracking and hold ability, increasing endurance time, and achieving good yaw control performance with different payloads and forward speeds.

1. Introduction

* Corresponding author.
E-mail address: crlae@nuaa.edu.cn (R. CHEN).

Production and hosting by Elsevier

In recent years, the concept and system of Urban Air Mobility (UAM) for urban low-altitude travel, transportation, and various special flight missions have gained much research attention.[1,2] One of the research directions of UAM is manned multi-rotor electric Vertical Takeoff and Landing (eVTOL)

aircraft due to its excellent vertical takeoff and landing performance, high safety redundancy, and low noise.[3,4]

However, recent simulations and flight tests in related literature [5–15] have shown that this type of aircraft is prone to actuator saturation during yaw control. Generally, the pitch and roll motions of a conventional multi-rotor eVTOL aircraft are controlled by the resultant moment generated by the multi-rotor thrust, and the yaw motion is controlled by the counter-torque differential between motors. Compared with conventional multi-rotor Unmanned Aerial Vehicles (UAV), manned multi-rotor aircrafts have specific characteristics of heavy load and high inertia. As a result, the yaw moment generated by the torque difference between motors has a more limited effect on the yaw angular acceleration of the aircraft. In other words, the yaw control efficiency of eVTOL aircraft is much lower than that of other control channels (lift, roll, and pitch), which can easily cause yaw controller saturation. This phenomenon can degrade the flight quality of the aircraft and even cause some motors to overheat, leading to aviation accidents. Therefore, it is necessary to alleviate or avoid the issue of yaw controller saturation for multi-rotor eVTOL aircraft, especially for a manned vehicle.

To date, many scholars have proposed various methods to address the problem of yaw controller saturation in multi-rotor eVTOL aircraft. One approach is to add constraints to prevent saturation from occurring. Weighted optimal control allocation[6] is one such method, which allocates control signals to ensure that actuators operate within a safe and effective range. Similarly, a fixed-time neural control scheme [7] with input and attitude constraints has been proposed, which utilizes a Neural Network (NN) anti-saturation auxiliary system to overcome adverse input saturation effects and introduces a Nonlinear State-Dependent Function (NSDF) to ensure that attitude constraint bounds are not violated. Another approach is to alleviate the effects of saturation to maintain flight performance. Event-triggered Reinforcement Learning (RL) control strategies[8] can stabilize quadrotor UAVs with actuator saturation, while the finite-time trajectory tracking control strategies[9] based on the Adaptive Dynamic Surface Control (ADSC) theory can enable UAVs to track the desired trajectories quickly and accurately. Other methods, such as extension Simple Adaptive Control (SAC),[10] dynamic anti-windup compensation[11,12] and adaptive quasi-sliding mode tracking control algorithms,[13] have also been used to handle input saturation effects and improve control performance. In addition to these approaches, some researchers propose adaptive neural fault-tolerant control schemes [14,15] that introduce auxiliary systems to handle actuator faults, external disturbances, and input saturation.

The control methods proposed in most literature can achieve satisfactory performance by avoiding or alleviating the issue of yaw controller saturation in multi-rotor eVTOL aircraft. However, the fundamental reason for this issue, the low efficiency of yaw control, is not addressed. There are relatively few studies that investigate the methods to improve the inherent effectiveness of yaw control from the perspective of configuration design.

Over the past five years, some eVTOL technology companies have implemented a rotor cross-tilt configuration method. By tilting the rotors, this technique utilizes the tangential component of rotor thrust to participate in yaw control, and effectively improves the yaw control efficiency of multi-rotor eVTOL aircraft. This configuration method has been utilized in various models such as DJI's S1000, Wisk Aero's Cora series, and Boeing's PAV, as shown in Fig. 1.

Nevertheless, there is a lack of public documentation or patents describing the rotor cross-tilt configuration to date. Therefore, it is worthwhile to further investigate an optimization method for the rotor cross-tilt mounting angle. This method can not only enhance the yaw control efficiency but also maintain the effectiveness of other control channels, thereby achieving optimal control performance overall. Meanwhile, it is important to consider the impact of this configuration on the aircraft's flight performance. Furthermore, to ensure practical applicability, a robust design should consider any potential errors in tilt mounting, and the variation of flight state.

This paper proposes a rotor cross-tilt mounting angle optimization method to address the intrinsic low yaw control efficiency of manned multi-rotor eVTOL aircraft. A 500-kg manned multi-rotor eVTOL aircraft designed and manufactured by a key research project in Zhejiang Province is used as a prototype, as shown in Fig. 2. The accuracy of the co-axial rotor model is verified using a single arm test bench, and the accuracy of the flight dynamics model is verified by the flight test data. Then, the rotor cross-tilt mounting angle optimization method is designed based on the flight dynamics model to not only improve the yaw control efficiency, but also basically maintain the efficiency of other control channels. The ideal rotor cross-tilt mounting angle for the prototype is determined by comprehensively considering the optimal results of rotor cross-tilt mounting angle with different loads, forward flight speeds, and rotor mounting angle errors. Finally, the feasibility of the rotor cross-tilt mounting angle is proved by analyzing the control derivatives of the flight dynamics model, the test data of a ground three Degree-of-Freedom (3DOF) platform, and the actual flight data of the prototype.

This research uses the open-source control code PX4 and the supporting ground station QGC (QGroundControl) to conduct various ground and flight tests on the manned multi-rotor eVTOL aircraft prototype. PX4 is a professional autopilot supported by an active world-wide community [16] and is most suitable for the design and test phase of the aircraft prototype of this study.

2. Flight dynamics modeling and validation

The aircraft's 8-axis and 16-propeller configuration limits its footprint while ensuring aerodynamic efficiency, making it an exceptionally safe option. Additionally, the aircraft's design includes more power redundancy, smaller blade diameter, and symmetric pitch and roll control, allowing it to maintain hovering even if any two propellers lose power. The basic parameters of the prototype are shown in Table 1.

2.1. Flight dynamics modeling

The aerodynamic force and torque of the rotor are calculated using the blade element theory, and the ground effect is considered according to the ground test data of a single co-axial rotor. The induced velocity calculation is based on the Pitt-Peters first-order harmonic dynamic inflow model. The lower rotor's inflow consists of a combination of its own induced

| (a) DJI's S1000 | (b) Wisk Aero's Cora series | (c) Boeing's PAV |

Fig. 1   eVTOL prototype with cross-tilt configuration.

Fig. 2   Prototype of manned multi-rotor eVTOL.

Table 1   Basic parameters of prototype.

Parameter	Value
Empty weight (kg)	374
Type of rotor	Tmotor P47*18 CF
Upper and lower rotor spacing (m)	0.34
No-load moment of inertia I_x, I_y, I_z (kg·m^2)	151, 150, 252
Body size (m)	$4.3 \times 4.3 \times 2$
Position of rotor platform	(0, 0, 0.27)
Aerodynamic center of fuselage (m)	(0, 0, 0)
Maximum one motor power (kW)	12
Rotor configuration	8 co-axial and co-rotating rotor systems, center symmetry

velocity and the upper rotor's induced velocity when the distance between the upper and lower rotors is close enough.[17] Then, the relationship between the thrust coefficient of the lower rotor and the induced velocity can be expressed as follows:

$$
\begin{cases}
C_{T,l} = 2v_{i0,l}\sqrt{\mu_l^2 + \left[\frac{w_{s,l}}{\Omega R} - (v_{i0,l} + v_{i0,u})\right]^2} \\
\mu_l = \frac{\sqrt{u_{s,l}^2 + v_{s,l}^2}}{\Omega R} \\
T_l = \rho \pi R^2 (\Omega R)^2 C_{T,l}
\end{cases}
\tag{1}
$$

where $C_{T,l}$ denotes the lower rotor thrust coefficient; $v_{i0,l}$ and $v_{i0,u}$ denote the dimensionless induced velocities of the lower and upper rotors, respectively; μ_l denotes the forward ratio; $(u_{s,l}, v_{s,l}, w_{s,l})$ denotes the velocity at the hub of the rotor; Ω denotes the rotor speed; R denotes the rotor radius; T_l denotes the lower rotor thrust; ρ denotes the local atmospheric density. The upper rotor is above the slipstream of the lower rotor,

resulting in an equivalent climb rate $v_{i0,ul}$ which is lower than the induced velocity $v_{i0,l}$. The speed ratio $v_{i0,ul}/v_{i0,l}$ is denoted as δ_{ul} ($\delta_{ul} < 1$). The Biot-Savart law is applied to simulate the streamline of the lower rotor, and the speed ratio δ_{ul} representing the interference acting on the upper rotor is yielded as follows: [18]

$$
\delta_{ul} = \frac{v_{i0,ul}}{v_{i0,l}} = 1 + \frac{-D_{lu}}{\sqrt{R^2\cos^2\chi + D_{lu}^2}}
\tag{2}
$$

where χ denotes the wake skew angle; D_{lu} denotes the distance between co-axial rotor hubs. The overall calculation flow chart of the co-axial rotor aerodynamics is shown in Fig. 3.

The aerodynamic interference between the multi-rotor system can significantly alter the flight dynamics characteristics across the flight range, which should be considered in the rotor modelling process. In this paper, the interaction among multi-rotor in forward flight is also modeled using the Biot-Savart law,[19] which assumes that the rear rotor operates in an additional uniform downwash induced by the front rotor. The rear rotor downward-induced velocity is calculated by considering a simple horseshoe vortex (see details in Ref. 19). The interference can be quantified by calculating the ratio k between the downward induced velocity at the center of the rear rotor and the induced velocity at the center of the front rotor.
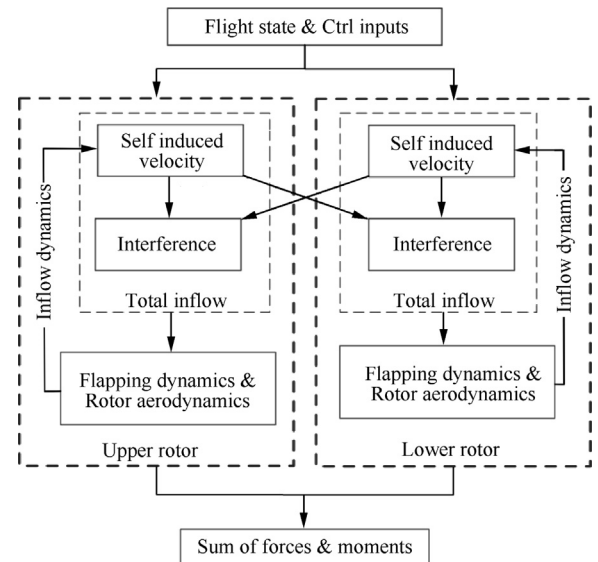

Fig. 3   Structure of co-axial rotor aerodynamics.

$$k = \frac{v_{iz,FR}}{v_{iz,F}} = \frac{p \cos \gamma + \sqrt{1 + \frac{p^2}{\cos^2 \alpha}} - p \tan \alpha \sin \gamma}{\sqrt{1 + \frac{p^2}{\cos^2 \alpha}}\left[1 + p^2 \cos^2 \gamma (\tan \alpha + \tan \gamma)^2\right]} \quad (3)$$

where α denotes the angle of attack of rotor disk; γ denotes the co-axial rotor wake skew angle; $p = l/R$; l denotes the distance between co-axial rotors; $v_{iz,FR}$ denotes the downward induced velocity at the center of the rear co-axial rotor; $v_{iz,F}$ denotes the induced velocity at the center of the front co-axial rotor. In order to improve computational efficiency, this study only considers the aerodynamic interference between the front and rear rotors during forward flight simulation, as shown in Fig. 4.

The dynamic characteristics of the prototype rotor flapping motion are closer to those of the co-axial rigid hingeless rotor due to the large size of the upper and lower rotor blades. An equivalent flapping hinge offset is generally used to simulate the flapping motion of a rigid hingeless rotor, and the equivalent flapping frequency and mode shape are ensured to be as close as possible to the real situation. Therefore, this paper adopts a method of combining an equivalent flapping hinge offset and an equivalent flapping torsion spring to construct a flapping motion model of the prototype rotor blade (Fig. 5). In Fig. 5, $\bar{e}$ denotes the dimensionless hinge offset; W denotes the flapping amplitude at $0.75R$; W_{tip} denotes the flapping amplitude at the tip.

$$\bar{e} = 1 - \frac{W_{tip}}{R \cdot \beta_{0.75}} \quad (4)$$

where $\beta_{0.75}$ denotes the flapping angle at $0.75R$ of the original blade. It is necessary to add an additional flapping torsion spring at the equivalent flapping hinge to keep the flapping frequency constant after equivalent flapping hinge offset. The stiffness of the torsion spring can be obtained according to the flapping frequency, as shown below:

$$K_\beta = \left(\bar{\omega}_n^2 - 1 - \frac{\bar{e} \, R M_\beta}{I_\beta}\right) I_\beta \Omega^2 \quad (5)$$

where K_β denotes the equivalent flapping torsion spring stiffness; I_β denotes the inertia moment of blade flapping; $\bar{\omega}_n$
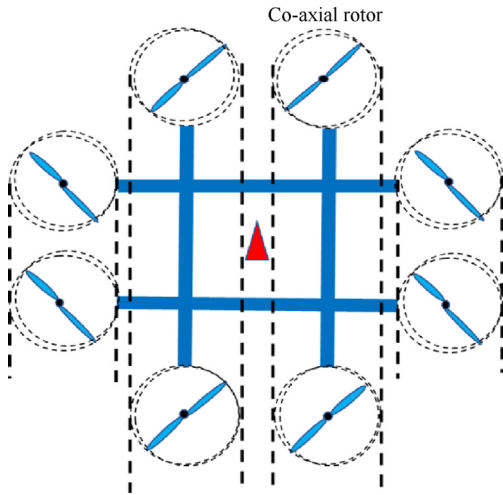

Fig. 4 Interactional diagram of front co-axial rotor wake to rear co-axial rotor.
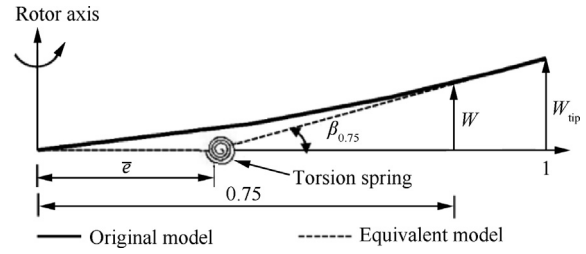

Fig. 5 Equivalent torsion spring approximation.

denotes the first-order flapping natural frequency of the dimensionless rotor; M_β denotes the mass moment of blade flapping. Thus, it can be ensured that the equivalent flapping frequency and the flapping mode are similar to the real situation.

According to the moment balance acting on the flapping hinge, the following blade flapping motion equation can be derived:

$$I_\beta \ddot{\beta} + K_\beta \beta + (I_\beta \cos \beta + e M_\beta)\Omega^2 \sin$$
$$\beta = \kappa \int_0^{R-e} \frac{1}{2} \rho a c (\Omega R)^2 \left(\bar{U}_T^2 \theta_G + \bar{U}_T \bar{U}_P\right) r' \mathrm{d}r'$$
$$+ 2(I_\beta + e M_\beta)(p_{HW}\Omega \cos \varphi' - q_{HW}\Omega \sin \varphi') +$$
$$I_\beta(\dot{p}_{HW}\sin \varphi' + \dot{q}_{HW}\cos \varphi') + M_\beta(\dot{w} - uq + pv - g) \quad (6)$$

where β denotes the blade flapping angle; e denotes the flapping hinge offset; k denotes the rotor tip loss coefficient; a denotes the blade lift line slope; c denotes the blade segment chord length; $\bar{U}_T$, $\bar{U}_P$ denote the blade profile normalized tangential and normal airflow velocities, respectively; θ_G denotes the blade profile pitch angle; r' denotes the radial length from the blade profile to the flapping hinge; p_{HW}, q_{HW} denote the hub roll and pitch angular velocities in the rotor wind axis system, respectively; φ' denotes the blade azimuth angle; u, v, w denote the velocities in the body axis system; p, q denote the roll and pitch angular velocities in the body axis system, respectively; g denotes the acceleration of gravity. By equating the constant term and the coefficient of the first harmonic term on the left and right sides of Eq. (6), the dynamics equation of the rotor disk in the wind shaft system can be derived as.

$$\begin{bmatrix} \ddot{a}_0 \\ \ddot{a}_1 \\ \ddot{b}_1 \end{bmatrix} + D \begin{bmatrix} \dot{a}_0 \\ \dot{a}_1 \\ \dot{b}_1 \end{bmatrix} + K \begin{bmatrix} a_0 \\ a_1 \\ b_1 \end{bmatrix} = f \quad (7)$$

where D denotes the damping matrix; K denotes the stiffness matrix; f denotes the extrinsic motivator vector; a_0, a_1, and b_1 denote the taper, rear, and side angles of the rotor disk, respectively (see details in Refs. 20,21).

The aerodynamic force and moment coefficients of the fuselage are obtained by interpolation of wind tunnel test data. The flight dynamics model is obtained by combining the dynamics equation of the rotor disk Eq. (7) with the rigid body kinematics equation, which can be expressed as follows:

$$\begin{cases} \dot{y} = f(y, u, t) \\ y = [y_F; y_R; y_I] \\ u = [\delta_c; \delta_{lat}; \delta_{lon}; \delta_p] \end{cases} \quad (8)$$

where y contains the fuselage state y_F, rotor state y_R, and inflow state y_I; u denotes the control vector, in which δ_c is the dimensionless thrust throttle input (0–1); δ_{lat} denotes the dimensionless roll control input (−1–1); δ_{lon} denotes the dimensionless pitch control input (−1–1); δ_p denotes the dimensionless yaw control input (−1–1); t denotes time.

In this paper, the control derivative $\partial M_z / \partial \delta_p$ of yaw moment M_z to yaw control input δ_p is used as an index to measure the yaw control efficiency. The larger the control derivative, the higher the control efficiency. The control derivatives of yaw, pitch, roll and vertical velocity can be extracted from the control derivative matrix, which is calculated by linearizing the nonlinear flight dynamics model (8) with the small disturbance hypothesis.[17] The linearized flight dynamics model can be established as

$$\Delta \dot{y} = A \Delta y + B \Delta u \tag{9}$$

where Δy denotes the state increment of the current state benchmark; Δu denotes the control increment of the current control benchmark; $\Delta \dot{y}$ denotes the first-order derivative of the state increment; A denotes the derivative matrix of the state quantity; B denotes the derivative matrix of the control quantity. The control derivative corresponding to each control channel can be obtained in the matrix B.

For the subsequent design process, a simulation platform of the multi-rotor eVTOL aircraft is established as shown in Fig. 6, where ω_m denotes the vector of all rotor rotation speeds. The platform includes the sensor noise module, battery module, rigid body dynamics, aerodynamics, actuator dynamics, and the turbulent wind field model based on Dryden.

The propellers are driven by brushless DC (BLDC) motors with the well-known mechatronic dynamics model.

$$\begin{cases} L_m \dot{I} = U - R_m I - k_e \Omega \\ J_m \dot{\Omega} = k_m I - \tau_d - k_v \Omega - k_s \end{cases} \tag{10}$$

where U and I denote the voltage and current of motor, respectively; R_m and L_m denote the resistance and inductance, respectively; J_m denotes the inertia of motor; k_e denotes the back Electromotive Force (EMF) constant; k_m denotes the electromagnetic torque constant; k_v denotes the viscous friction constant; k_s denotes the solid friction constant; τ_d denotes the load of motor which can be obtained from aforementioned aerodynamics of rotor.

2.2. Validation

The accuracy of the co-axial rotor model is verified using a single arm test bench. The thrust and output power of the upper and lower rotors are measured using the tension meter, torsion

meter, and the laser velocimeter. The test results are compared with the calculated results of the co-axial rotor model. Fig. 7 shows that the co-axial rotor model can describe the actual rotor aerodynamics well.

The steady forward flight of the prototype with empty payload is calculated and compared with the test data of the latest version of the prototype, as shown in Fig. 8. The test environment was as follows: Hangzhou Nanhu test flight site, 20 m above the ground, level 1 wind (0.3–1.5 m/s), standard atmospheric pressure, and fully charged before takeoff. The trim results of the prototype flight dynamics model established in this paper agree well with the flight test results.

The simulation platform is verified using maneuver forward flight test data, as shown in Fig. 9. The flight test took place at the Nanhu test flight site in Hangzhou, with a forward speed command of 6 m/s, a height of 30 m above the ground as commanded by ground station QGC, level 3 wind (3.4–5.4 m/s), standard atmospheric pressure, and fully charged before takeoff. The flight test data and simulation results are compared and analyzed. The forward flight speed, pitch angle, thrust control input, and pitch control input, which strongly influence the forward flight scenario, are presented in Fig. 9. The results demonstrate highly consistent maneuvering and steady states between the experiment and simulation, confirming that the simulation platform established in this paper is accurate.

3. Rotor cross-tilt mounting angle optimization method

This paper proposes a rotor cross-tilt mounting angle optimization method, which uses the tangential component of rotor thrust to improve the yaw control performance. In addition, this method also aims to maintain the control efficiency of the original lift, pitch, and roll channels to achieve the overall optimal control performance.

Fig. 10 shows a schematic diagram of rotor cross-tilt configuration for the prototype multi-rotor eVTOL aircraft, where β_m denotes the rotor cross-tilt angle; T denotes the co-axial rotor thrust; l_x denotes the normal distance between the lateral force F_t and the center of gravity, and l_y denotes the vertical distance. The lateral component of co-axial rotor thrust F_t generates an auxiliary yaw moment N_a on the center of gravity of the fuselage. In this paper, the prototype adopts the configuration of co-axial rotor, and the upper and lower rotors rotate in the same direction (co-rotating). Therefore, the auxiliary yaw moment is always in the same direction as the negative torque of the co-axial rotor (the co-rotating configuration makes the negative torque direction of the co-axial rotor fixed), and this helps improve the yaw control efficiency of the aircraft.
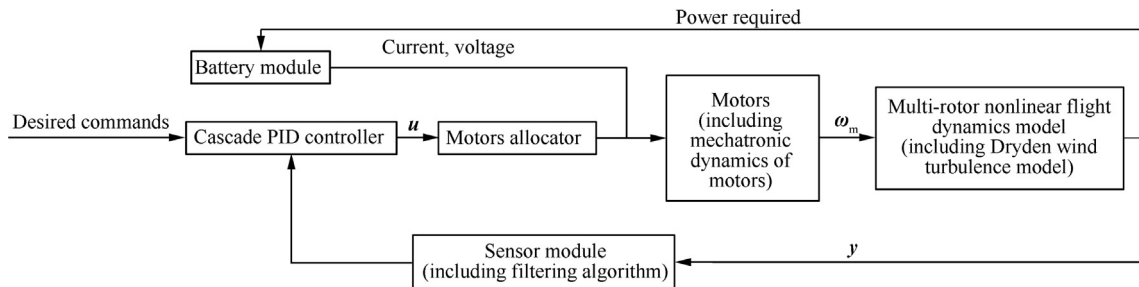

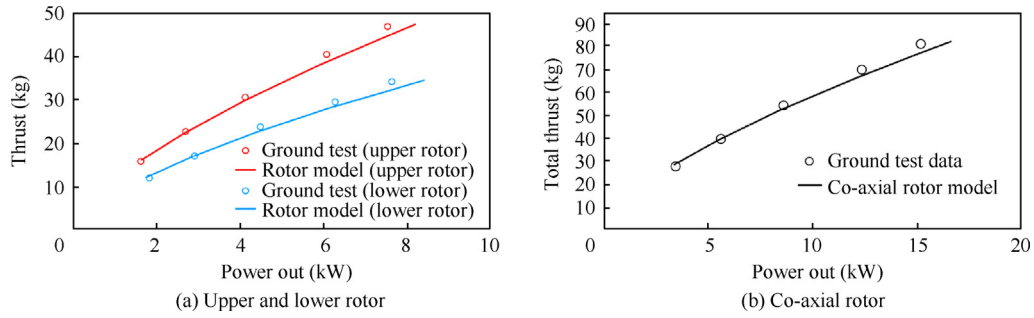**Fig. 6** Simulation platform for multi-rotor eVTOL.

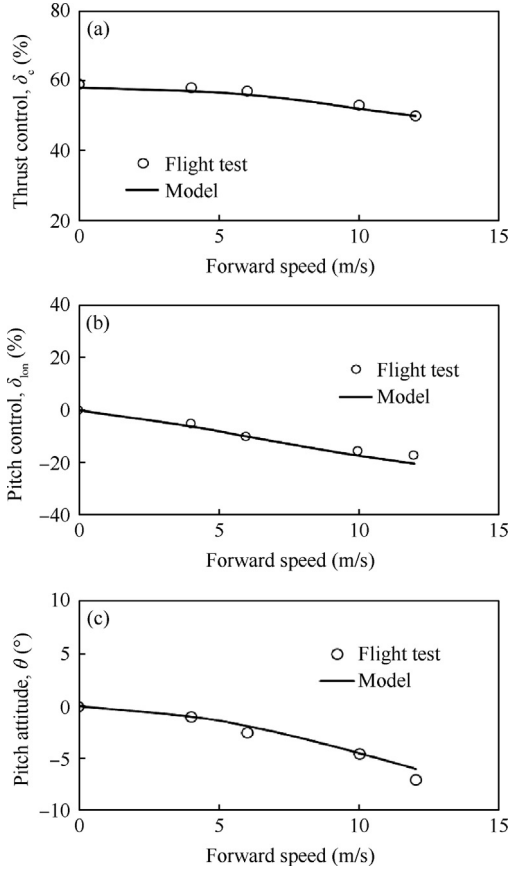**Fig. 7** Thrust and power of co-axial rotor vs test data.

Fig. 8 Prototype simulation vs steady-level flight test.

In a multi-rotor eVTOL aircraft, the lateral and longitudinal moments are generated by the thrust from the rotors, and the yaw motion is controlled by the counter-torque differential. Here, considering the central symmetry of the aircraft, only lateral-relevant moments and forces are discussed. The yaw and lateral moments (N and L respectively) acting on the multi-rotor aircraft without cross-tilt angle is yielded as

$$N = Q_1 - Q_2 + Q_3 - Q_4 + Q_5 - Q_6 + Q_7 - Q_8$$

$$= \sum_{i=1}^{4} (Q_{(2i-1)} - Q_{(2i)}) \tag{11}$$

$$L = (T_1 + T_6 - T_2 - T_5)l_y + (T_7 + T_8 - T_3 - T_4)l_x \tag{12}$$

where $Q_i(i = 1, 2, \cdots, 8)$ refers to the torque from each co-axial rotor system.

The additional torque generated from the tangential force from the rotor cross-tilt angle is added as follows:

$$N = \sum_{i=1}^{4} (Q_{(2i-1)} - Q_{(2i)}) \cos \beta_m + \sum_{i=1}^{4} (T_{2i-1} - T_{2i})l_x \sin \beta_m$$

$$\tag{13}$$

$$L = (T_1 + T_6 - T_2 - T_5)l_y \cos \beta_m + (T_7 + T_8 - T_3 - T_4)l_x \cos \beta_m$$

$$\tag{14}$$

Then, the possible coupling resulted from the tilted rotor is analyzed. Yaw control leads to additional tangential components of propeller thrust, resulting in the lateral force as

$$F_{y,yaw} = (T_1 - T_2 - T_5 + T_6) \sin \beta_m \tag{15}$$

Considering the central symmetry characteristics of the aircraft, as shown in Fig. 10, the lateral force is near zero in yaw control.

Furthermore, a lateral (roll) control also introduces additional lateral forces, which can be expressed as

$$F_{y,roll} = (T_1 + T_6 - T_2 - T_5) \sin \beta_m \tag{16}$$

The lateral forces contribute to the total lateral moments, represented by

$$L = (T_1 + T_6 - T_2 - T_5)l_y \cos \beta_m + (T_7 + T_8 - T_3 - T_4)l_x \cos \beta_m + F_{y,roll}h_{cg} \tag{17}$$

where h_{cg} refers to the height of the rotor above the aircraft center of gravity. As indicated by Eq. (17), the additional force $F_{y,roll}$ benefits the corresponding lateral control.

According to Fig. 10 and Eqs. (13)–(17), a tiny rotor cross-tilt angle has limited effect on improving the yaw control efficiency, while an excessively large cross-tilt angle can significantly increase the lift throttle, reduce the control efficiency of other attitude control channels, and even lead to control difficulties and arm lateral structural strength problems. Therefore, it is necessary to find an ideal rotor cross-tilt mounting angle for the prototype.

In practical application, there are unavoidable installation errors. Therefore, the rotor mounting angle error e_θ is also considered in rotor cross-tilt mounting angle optimization. Fig. 11 shows a schematic diagram of rotor mounting angle error e_θ for the prototype multi-rotor eVTOL aircraft, where F_e denotes the lateral component of co-axial rotor thrust T due to the rotor mounting angle error $e_{\theta i}$ ($i = 1,2,...8$) of
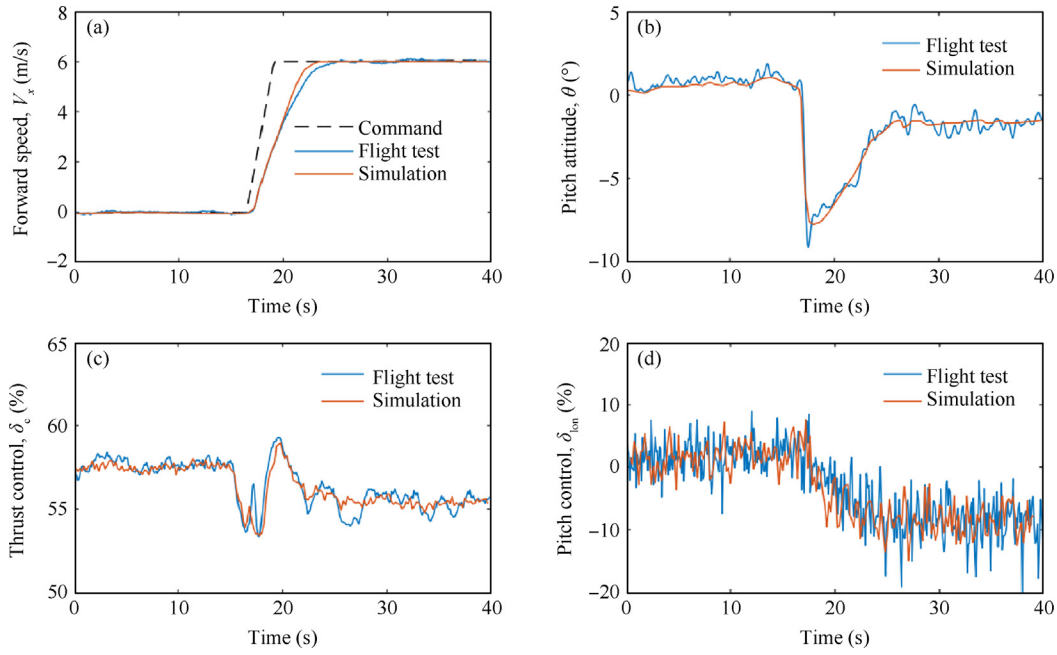
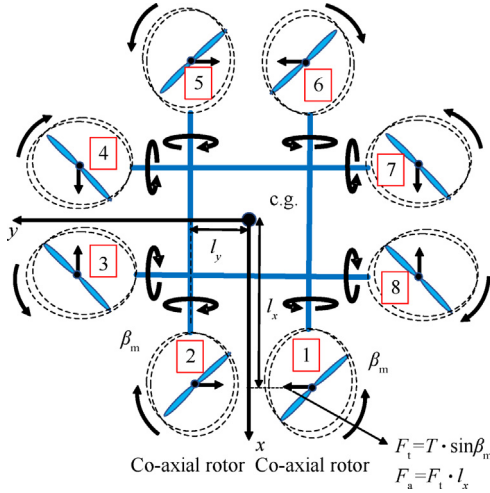**Fig. 9** Prototype simulation vs speed command (6 m/s) tracking flight test.

Fig. 10 Rotor cross-tilt configuration.

Fig. 11 Rotor mounting angle error e_θ for each co-axial rotor.

the 8 co-axial rotors. The lateral force F_e generates an extra yaw moment N_e on the center of gravity of the fuselage, which may reduce the yaw control efficiency of the aircraft. The conventional rotor radial mounting error is found to have little influence on the three-attitude control performance of the multi-rotor eVTOL aircraft. Therefore, this paper only considers the rotor tangential mounting angle error, and a positive error is defined as generating positive torque moment.

The final torque moment considering the influence of the mounting angle error is as follows:

$$N = \sum_{i=1}^{4} \left[N_{a(2i-1)} = \cos(\beta_m + e_{\theta(2i-1)}) - N_{a(2i)} \cos(\beta_m - e_{\theta(2i)}) \right]$$

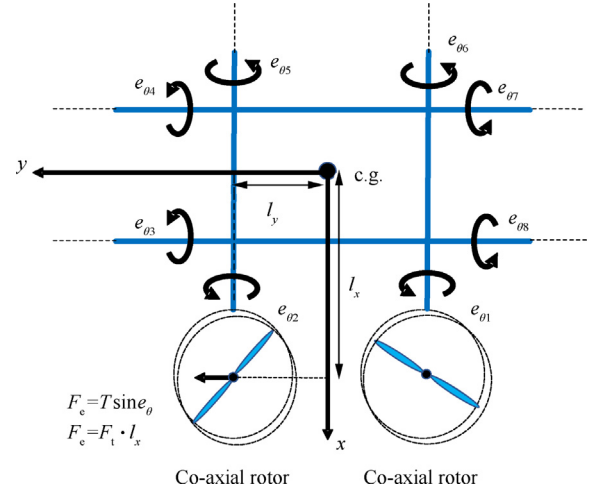$$+ \sum_{i=1}^{4} \left[T_{2i-1} l_x \sin(\beta_m + e_{\theta(2i-1)}) - T_{2i} l_x \sin(\beta_m - e_{\theta(2i)}) \right]$$

$$\tag{18}$$

Based on the manufacturing process of the prototype and the actual measurement results before and after hundreds of flight tests, the optimization calculation proposed in this paper introduces the following two kinds of tolerance ranges:

(1) Conventional error range: the absolute value of the total rotor mounting angle error on the eight arms cannot exceed $4.8°$ ($\sum_{i=1}^{8} |e_{\theta i}| \leqslant 4.8°$). In other words, the absolute value of the rotor mounting angle error on each arm cannot exceed $0.6°$ on average ($|e_{\theta i}| \leqslant 0.6°$, $i = 1, 2, \cdots, 8$).

(2) Large error range: the absolute value of the total rotor mounting angle error on the eight arms cannot exceed $8°$ ($\sum_{i=1}^{8} |e_{\theta i}| \leqslant 8°$). In other words, the absolute value of the rotor mounting angle error on each arm cannot exceed $1°$ on average ($|e_{\theta i}| \leqslant 1°$, $i = 1, 2, \cdots, 8$).

This paper focuses on designing the optimal rotor cross-tilt mounting angle for steady flight states of the aircraft, such as hovering and forward flight, which involves trim calculation and cross-tilt angle optimization. Therefore, a numerical optimization method that can simultaneously complete both trim calculation and optimization is proposed to obtain the optimal rotor cross-tilt angle in specified flight tasks and rotor mounting angle errors. The calculation process is illustrated in Fig. 12.

In order to balance the power consumption of each control input and achieve the optimal overall flight performance, the objective function is defined as the minimum sum of squares of the total control inputs of the aircraft. This approach aims to achieve an optimal balance of control inputs while minimizing power consumption and enhancing flight performance.

$$\min_{\beta_m} J_A = w_1\delta_c^2 + w_2\delta_{lat}^2 + w_3\delta_{lon}^2 + w_4\delta_p^2 \qquad (19)$$

s.t.

$$\beta_{m,min} \leqslant \beta_m \leqslant \beta_{m,max} \qquad (20)$$

where $w_1 - w_4$ denote the weight coefficients. The control weights of the four channels are equally important, so w_1–w_4 is considered as 0.25. The available range of the rotor cross-tilt angle ($\beta_{m,min}$–$\beta_{m,max}$) is set between $-30° - 30°$, and the initial value β_m of the iteration is 0°.

During each optimization iteration, the algorithm updates the cross-tilt mounting angle and performs a trim calculation using the flight dynamics model updated with the current flight mission, rotor installation angle error, and cross-tilt mounting angle. The trim calculation yields the corresponding control variables, which are then employed to calculate the objective function J_A until the convergence is achieved. In the trim calculation, the resultant force and moment acting on the aircraft are balanced, so the angular velocity (p, q, r), linear acceleration ($\dot{u}, \dot{v}, \dot{w}$), and angular acceleration ($\dot{p}, \dot{q}, \dot{r}$) terms of the aircraft are all equal to 0.

$$\begin{cases} p = 0, q = 0, r = 0 \\ \dot{u} = 0, \dot{v} = 0, \dot{w} = 0, \dot{p} = 0, \dot{q} = 0, \dot{r} = 0 \\ \dot{\boldsymbol{p}} = \boldsymbol{V}_d \end{cases} \qquad (21)$$

where $\boldsymbol{p}$ denotes the position in the earth axis, and $\boldsymbol{V}_d$ denotes the expected speed of the flight mission.

In addition, the flapping motion of each rotor is also in a steady state.

$$\boldsymbol{K}\begin{bmatrix} a_0 \\ a_1 \\ b_1 \end{bmatrix} - \boldsymbol{f} = \boldsymbol{0} \qquad (22)$$

The trim calculation and rotor cross-tilt optimization are solved by the robust sequential quadratic programming algorithm [22] and the golden section method, respectively.
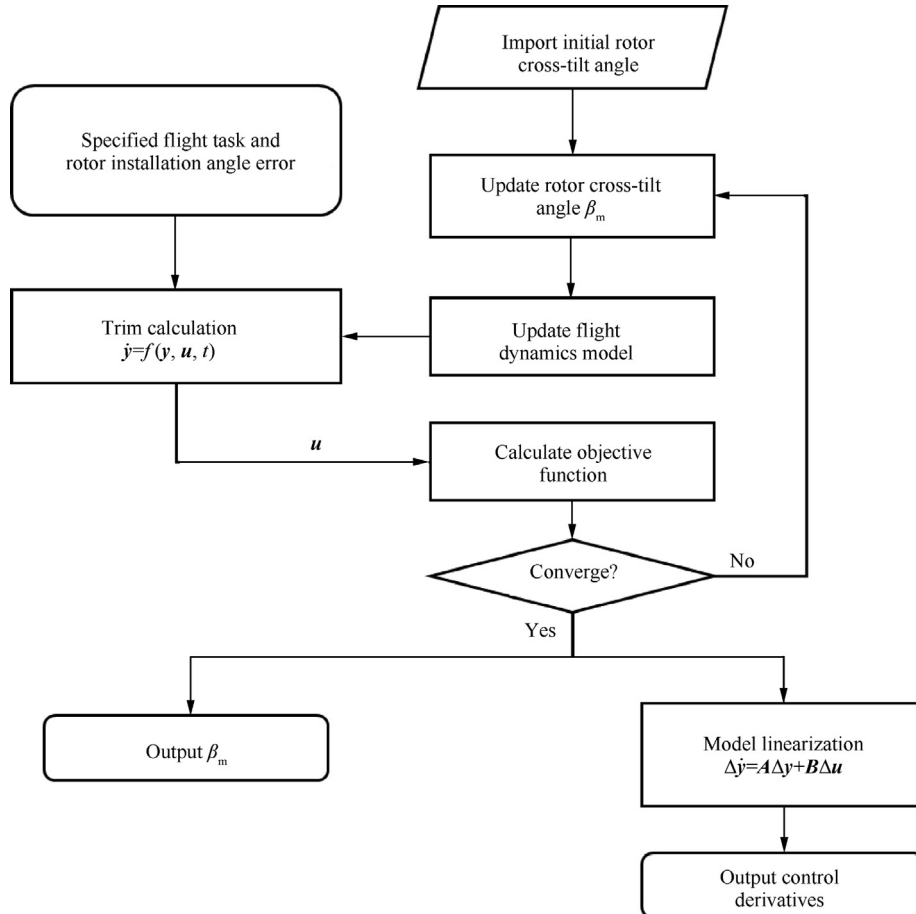

Fig. 12 Schematic diagram of rotor cross-tilt mounting angle optimization method.

This paper uses the control derivative as a metric to measure the control efficiency. The larger the control derivative, the higher the control efficiency. The control derivatives of yaw, pitch, roll and vertical velocity can be extracted from the control derivative matrix $\boldsymbol{B}$, which is calculated by the linearized flight dynamics model Eq. (9).

The 500-kg manned multi-rotor eVTOL prototype is used to calculate the optimal rotor cross-tilt mounting angle with different takeoff weights, forward flight speeds and rotor installation angle errors. The optimization results are shown in Tables 2 and 3.

According to Tables 2 and 3, the optimal rotor cross-tilt mounting angle varies with different payloads, forward flight speeds, and rotor mounting angle errors. With the increase of the rotor installation error, the aircraft experiences a larger extra adverse yaw moment, which requires a larger rotor cross-tilt mounting angle to counteract the adverse effect. In addition, the optimal rotor cross-tilt angle also gradually increases with the forward flight speed and payload. This is because the yaw control derivative $\partial M_z / \partial \delta_p$ of the yaw moment M_z to the yaw control input δ_p gradually decreases with the increase in forward flight speed and weight, as shown in Fig. 13. Thus, a larger rotor cross-tilt angle is required to help improve the yaw control efficiency.

As shown in Fig. 14(a), after optimization, the yaw control derivative $\partial M_z / \partial \delta_p$ is greatly improved (increased by 200%), indicating the improvement of yaw control efficiency. Fig. 14 (b) shows the roll control derivative $\partial M_x / \partial \delta_{lat}$ (the pitch control derivative is similar to the case of roll due to the central symmetric configuration of the prototype). The lift channel is represented by the vertical control derivative $\partial V_z / \partial \delta_c$ of the vertical velocity V_z to the thrust control input δ_c. It can be seen from Fig. 14(b) that the optimal rotor cross-tilt mounting angle has little effect on the thrust and roll channels, so that the overall optimal control performance is achieved.

According to the parameter analysis in Tables 2 and 3, it can be found that within a certain range of rotor installation angle error, payload, and flight speed (taking the prototype as an example, the average rotor installation error of 0°–1°, payload of 0–80 kg, and speed of 0–6 m/s), the optimal rotor cross-tilt mounting angle does not vary significantly (3.43°–6.86°). If we take the average of all the optimal solutions within this range as a fixed rotor cross-tilt mounting angle (5°), it is found that the deviation of each control derivative from its optimal value will not exceed 2.5%, which can also lead to good overall flight performance.

From an engineering perspective, it is impractical to develop a drive device for the multi-rotor aircraft that needs to adaptively adjusts the rotor cross-tilt angle according to the payload and flight speed, considering the additional drive equipment weight, as well as the costs of modifying the structure and power system. Fortunately, based on the above theo-

Table 2 Results of rotor cross-tilt optimization ($e_\theta = 0.6°$).

Load (kg)	Forward speed		
	0 m/s	4 m/s	6 m/s
0	3.43°	3.63°	4.01°
40	3.85°	4.01°	4.29°
80	4.38°	4.53°	4.78°

Table 3 Results of rotor cross-tilt optimization ($e_\theta = 1°$).

Load (kg)	Forward speed		
	0 m/s	4 m/s	6 m/s
0	4.91°	5.22°	5.80°
40	5.47°	5.72°	6.18°
80	6.18°	6.43°	6.86°
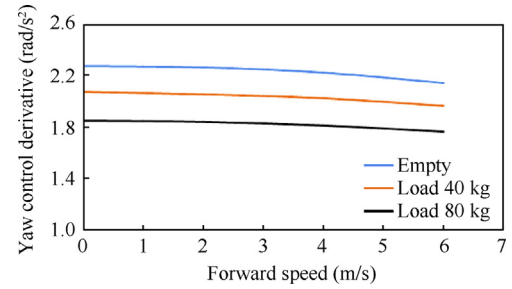
Fig. 13 Yaw control derivatives with different speeds and loads before optimization.

retical analysis, it can be concluded that an ideal yaw control effect can be also achieved using a fixed rotor cross-tilt mounting angle (as shown in Fig. 15). The ground and flight test data introduced in the following Section 4 will also demonstrate this point very well. This conclusion has great significance in engineering application.

4. Ground and flight tests

In this paper, the feasibility and application value of the optimization result are further illustrated by the test data of the three Degrees of Freedom (3DOF) rotor platform and the actual flight test data of the prototype before and after rotor cross-tilt optimization.

### 4.1. Ground 3DOF rotor platform test analysis

This paper conducts yaw hold and yaw slope command tracking tests on a 3DOF rotor platform, and compares the results before and after rotor cross-tilt optimization. The 3DOF rotor platform is shown in Fig. 16.

Fig. 17 shows a comparison of the yaw hold command test data of the prototype 3DOF rotor platform. As shown in Fig. 17, under the yaw hold command, the yaw control amount δ_p after rotor cross-tilt optimization decreased significantly (variance decreases by 70% and maximum amplitude decreases by 58%), and the amplitude of the yaw rate fluctuation is reduced by 50% on average.

Fig. 18 shows a comparison of the yaw slope command (12 (°)/s) test data of the prototype 3DOF rotor platform. As shown in Figs. 18(a) and (c), the yaw angle tracking performance after rotor cross-tilt optimization is better under the yaw slope command (12 (°)/s), and the maximum error is reduced by 40%. A comparison of Figs. 18(b) and (d) shows that the yaw control amount δ_p after optimization has an
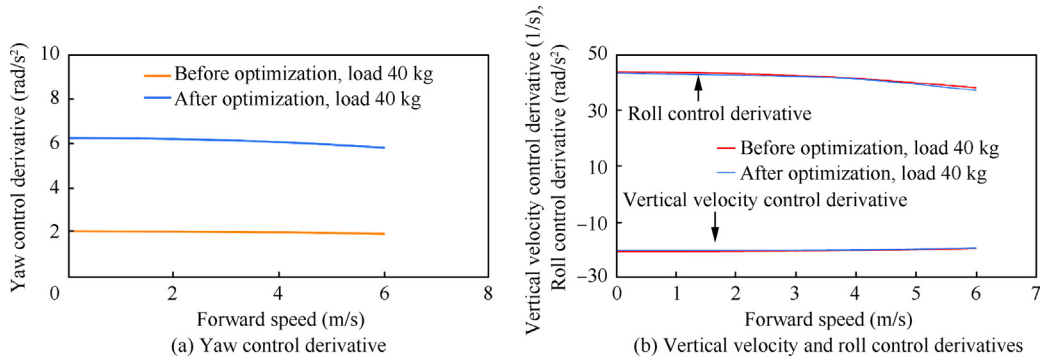
Fig. 14 Comparison of control derivatives before and after optimization.
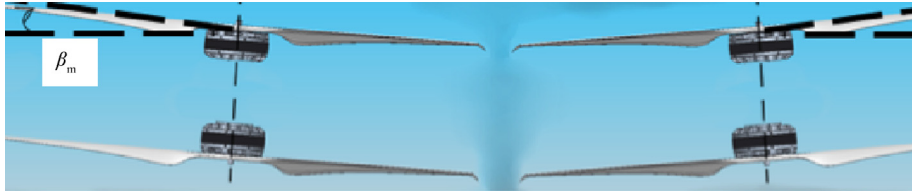
Fig. 15 Schematic diagram of rotor cross-tilt mounting.
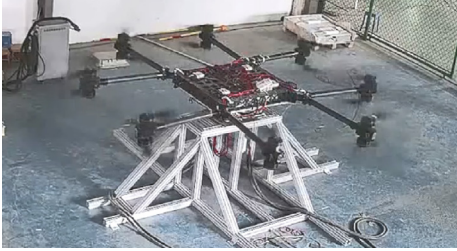
Fig. 16 3DOF rotor platform.

amplitude of close to 10% at the beginning and end of the slope command, and then immediately returns to 0%. In addition, the pitch and roll tracking performance of the prototype rotor platform remains unchanged, so these test results are not compared here.

4.2. Prototype hovering flight test analysis

Hovering flight tests are used to validate that the rotor cross-tilt mounting angle can achieve good yaw control performance under different payloads, as shown in Fig. 19. The test environment of the two groups of data is the same, i.e., the Nanhu test flight site in Hangzhou, 2 m above the ground, level 3 wind, standard atmospheric pressure, and fully charged before takeoff. In this paper, the flight test data are compared and then analyzed.

Fig. 20 shows a comparison of the hovering flight test data of the prototype with empty payload. With rotor cross-tilt of 5°, the maximum tracking error is reduced from 7.5° to within 3°, and the yaw control δ_p used to maintain the yaw attitude is significantly reduced (variance decreases by 65%, and the maximum amplitude decreases by 50%).

Fig. 21 shows a comparison of the 70-kg payload hovering flight test data of the prototype between no rotor cross-tilt and

5° rotor cross-tilt. As shown in Fig. 21(a), it is difficult to maintain the yaw attitude under a payload of 70 kg with no rotor cross-tilt. The maximum tracking error reaches nearly 60°. In Fig. 21(b), the yaw control is too high, and is almost saturated throughout the process. As flight time increases, the battery voltage decreases, requiring increased thrust throttle to maintain lift, which reduces the throttle margin available for attitude control. Consequently, after 6.5 min, the aircraft becomes unable to sustain yaw attitude. In compliance with our pre-established safety measures, the aircraft will initiate an automatic landing. It can be seen that under a heavy payload condition, the additional yaw moment caused by the rotor mounting angle error increases, resulting in the issues such as difficulty in maintaining the yaw attitude, easy capping of the throttle, and decline of endurance time.

As shown in Figs. 21(c) and (d), the yaw tracking performance is significantly improved at rotor cross-tilt of 5°, with the maximum tracking error of 4.5° only. The yaw control amount δ_p required to maintain the yaw is significantly reduced and basically maintained within 5%. In accordance with our pre-established safety measures, the aircraft will initiate an automatic safe landing when the remaining battery level reaches 10% State of Charge (SOC).

Table 4 shows a comparison of the actual hovering duration time of the prototype under different payloads with no rotor cross-tilt and 5° rotor cross-tilt. As shown in Table 4, the endurance time of the manned multi-rotor eVTOL developed in this project has been extended due to the significant reduction in the proportion of yaw control amount. In other words, the greater the load, the more obvious the improvement in endurance time.

Furthermore, from Table 4, it is notable that when the load is 30 kg, the endurance time improvement is 5.9%. However, when the load is 70 kg, the endurance time improvement is 84.6%. This is because when the load is 30 kg, both configurations of "No rotor cross-tilt" and "Rotor cross-tilt of 5°" yield
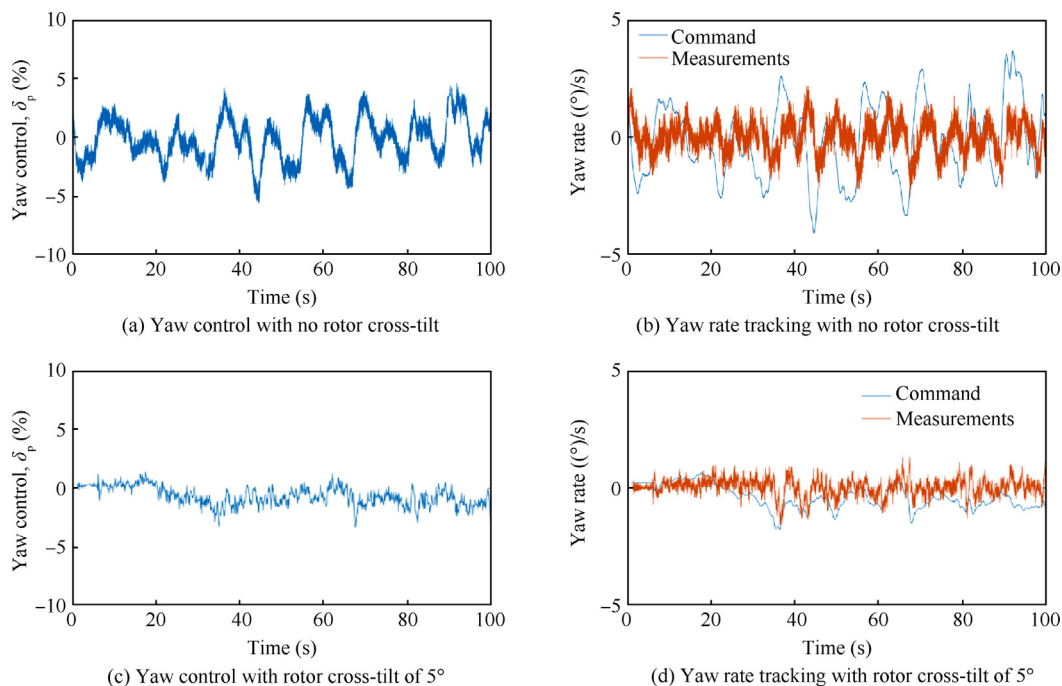
(a) Yaw control with no rotor cross-tilt

(b) Yaw rate tracking with no rotor cross-tilt

(c) Yaw control with rotor cross-tilt of 5°

(d) Yaw rate tracking with rotor cross-tilt of 5°

Fig. 17 Comparison of yaw hold command test data of prototype 3DOF rotor platform.

(a) Yaw slope command tracking, no rotor cross-tilt

(b) Yaw control with no rotor cross-tilt

(c) Yaw slope command tracking, rotor cross-tilt of 5°

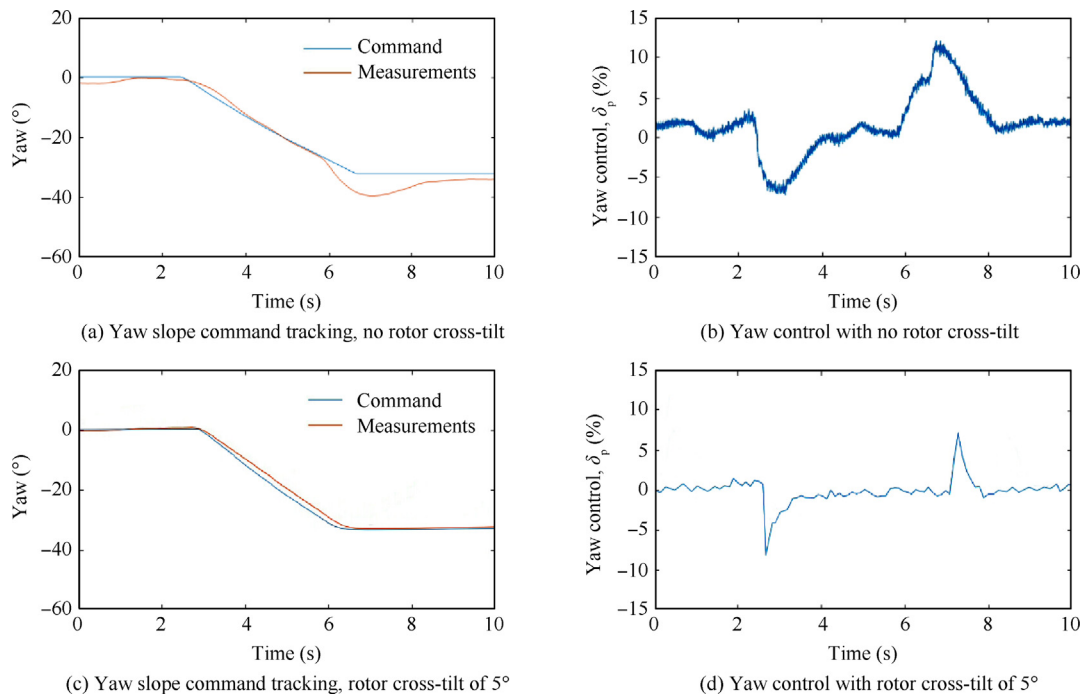(d) Yaw control with rotor cross-tilt of 5°

Fig. 18 Comparison of yaw slope command test data of prototype 3DOF rotor platform.

similar remaining battery levels, leading to a modest 5.9% improvement in endurance time. On the other hand, when the load is 70 kg, without rotor cross-tilt, the aircraft is unable to maintain its yaw attitude when the battery has only discharged 50% (SOC 50%), necessitating a landing. With the implementation of rotor cross-tilt, the aircraft can hover until it reaches a safe remaining battery level (SOC 10%) before landing. Hence, the endurance time improvement is significantly higher at 84.6% in this case. It is worth noting that during each test flight, there may be unavoidable variations in rotor mounting angle errors and the surrounding wind field, which can affect the flight time of the aircraft. For example, when flying with an empty load, the endurance time improvement is 8.3%.

Fig. 19 Prototype hovering flight test.

4.3. Prototype trajectory tracking test analysis

The trajectory tracking tests are used to validate that the rotor cross-tilt mounting angle can achieve good yaw control performance at different forward speeds, as shown in Fig. 22. The test environment of the two groups is the same, i.e., the Nanhu test flight site in Hangzhou, 30 m above the ground, level 3 wind, standard atmospheric pressure, no payload, fully charged before takeoff, and the same trajectory command ordered by ground station QGC. The flight position and control data are presented in Fig. 23.

During forward flight, the yaw control derivative decreases with increasing speed (as shown in Fig. 13), indicating a decrease in yaw control efficiency. Consequently, more yaw control input is required during forward flight. In this study, the rotor cross-tilt optimization method is employed to increase the yaw control derivative of the prototype by 200% compared to its original value (as illustrated in Fig. 14). This significant increase in the yaw control derivative results in a notable improvement in yaw control efficiency, thereby reducing the amount of yaw control input required during forward flight. As shown in Fig. 23, when tracking the same trajectory, the manned multi-rotor eVTOL prototype

exhibits consistent trajectory tracking performance with both configurations of "no rotor cross-tilt" and "5° rotor cross-tilt". In comparison, the yaw control amount δ_p is reduced by an average of 7% with 5° rotor cross-tilt, and other control channels are almost the same. Considering the previous results from hover tests, it can be concluded that the cross-tilt optimization method can improve yaw control efficiency during both hovering and forward flights.

5. Conclusions

Manned multi-rotor eVTOL aircraft exhibits requirements for stronger power, larger structure size, and higher payload. Under the condition of heavy payload, the problem of yaw control actuator saturation is prominent. At present, the research on yaw anti-saturation of multi-rotor eVTOL aircraft mainly focuses on improvement of control law, which cannot fundamentally solve the problem of weak yaw control effectiveness. Therefore, this paper investigates a rotor cross-tilt mounting angle optimization method, which can not only improve the yaw control efficiency but also maintain the efficiency of other control channels, so as to achieve the overall optimal control performance. A 500-kg manned multi-rotor eVTOL aircraft is used as a prototype, and then a rotor cross-tilt mounting angle optimization method is designed to maximize the overall control efficiency with different loads, forward flight speeds, and rotor installation angle errors. Through theoretical analysis and experimental verification, this paper draws the following conclusions.

(1) The manned multi-rotor eVTOL flight dynamics model established in this paper is relatively accurate, and the flight simulation platform developed based on it can effectively predict the steady and maneuver forward flight of the prototype.

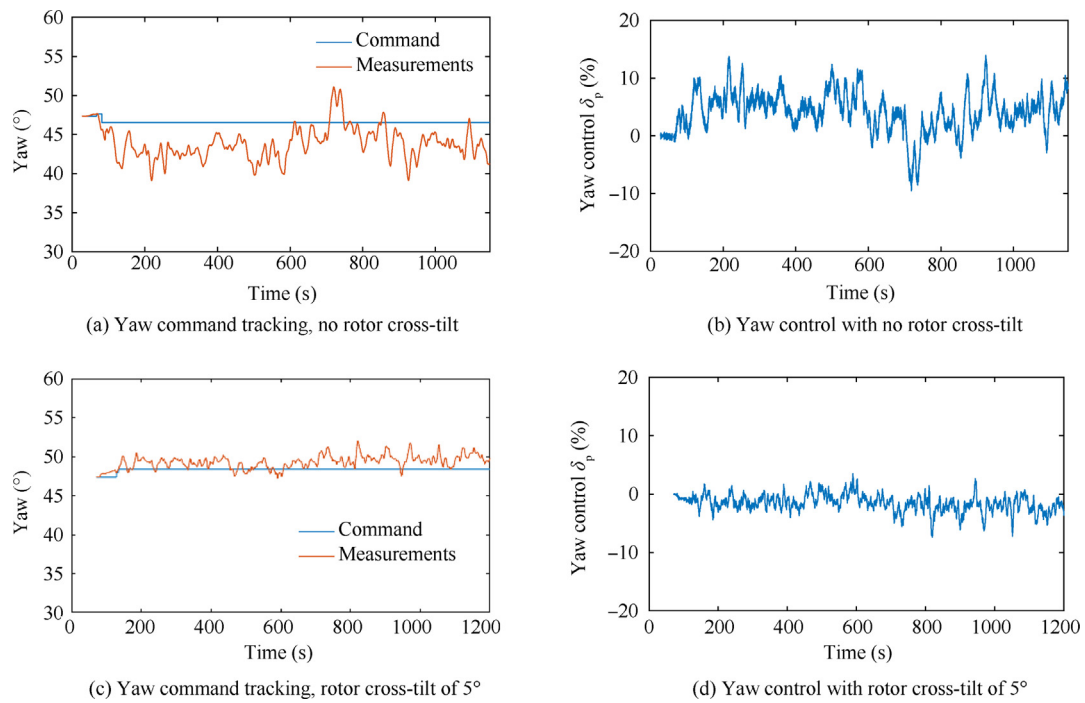(a) Yaw command tracking, no rotor cross-tilt

(b) Yaw control with no rotor cross-tilt

(c) Yaw command tracking, rotor cross-tilt of 5°

(d) Yaw control with rotor cross-tilt of 5°

Fig. 20 Comparison of prototype hovering flight test data with empty payload.

(a) Yaw command tracking, no rotor cross-tilt

(b) Yaw control with no rotor cross-tilt

(c) Yaw command tracking, rotor cross-tilt of 5°

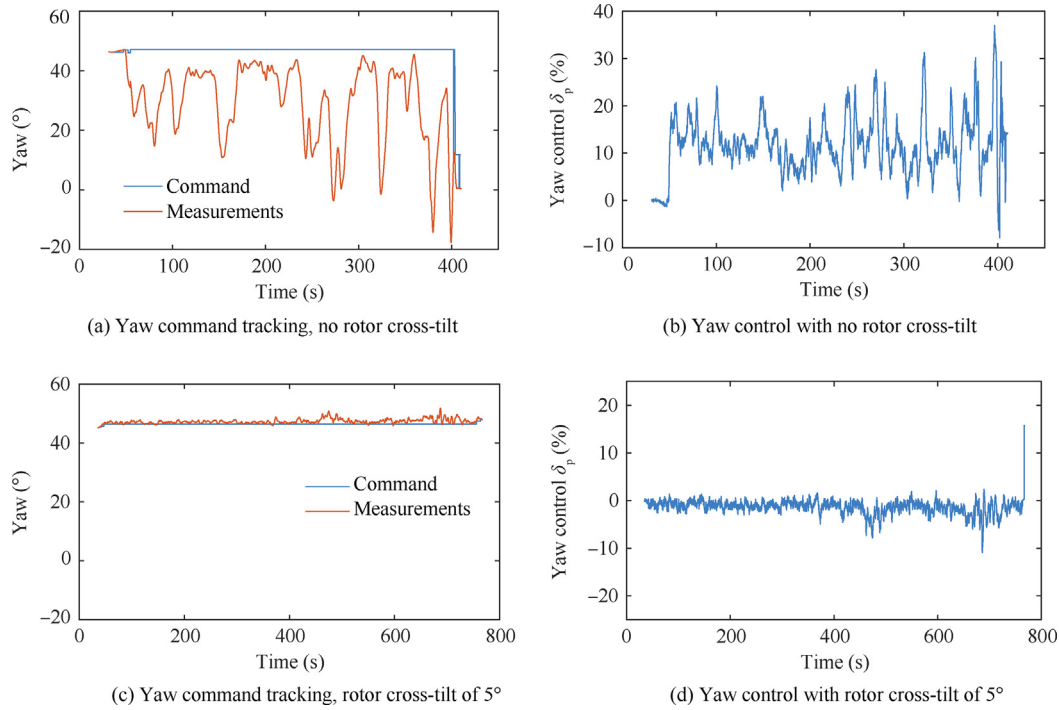(d) Yaw control with rotor cross-tilt of 5°

Fig. 21 Comparison of prototype hovering flight test data with 70-kg payload.

Table 4 Endurance comparison.

| Load (kg)	No rotor cross-tilt		Rotor cross-tilt of 5°		Improvement
	Endurance (min)	Reason for landing	Endurance (min)	Reason for landing	
0	18.5	Saturation of yaw control, SOC 15%	20	Battery SOC 10%	↑ 8.3 %
30	17	Saturation of yaw control, SOC 15%	18	Battery SOC 10%	↑ 5.9 %
70	6.5	Saturation of yaw control, SOC 50%	12	Battery SOC 10%	↑ 84.6%
100	3.6	Saturation of yaw control, SOC 60%	6.5	Battery SOC 10%	↑ 80.5%

Fig. 22 Prototype trajectory tracking test.

(2) The aircraft experiences a larger adverse yaw moment with an increase in the rotor installation error, requiring a larger rotor cross-tilt mounting angle to counteract the effect. Moreover, the optimal rotor cross-tilt mounting angle gradually increases with an increase in forward flight speed and payload. This is due to varying control variables and their derivatives under different conditions.

(3) Within a certain range of rotor installation angle error, payload, and flight speed, the optimal rotor cross-tilt mounting angle does not vary significantly, with devia-tion of the control derivative from its optimal value below 2.5%. This indicates the feasibility of a practical application for a fixed rotor cross-tilt mounting angle. In addition, ground and flight tests show that a fixed angle can achieve ideal yaw control and good overall flight performance.

(4) Yaw control derivative is significantly improved by 200% after optimization, and the efficiency of other control channels are maintained according to theoretical simulation and flight tests. The improved yaw control efficiency results in better yaw hold and tracking ability under different payloads in the hover state and trajectory command tracking tests under different forward speeds. Endurance time is also increased, particularly at heavy payloads.

(5) This study has certain limitations that should be noted. Firstly, it only explores a single type of manned multi-rotor eVTOL aircraft, and further research is necessary to validate whether the findings are transferable to other aircraft types. Secondly, the effect of the optimal rotor cross-tilt mounting angle on the aircraft's wind resis-tance and maneuverability has not yet been investigated

(a) Position comparison

(b) Control channel comparison
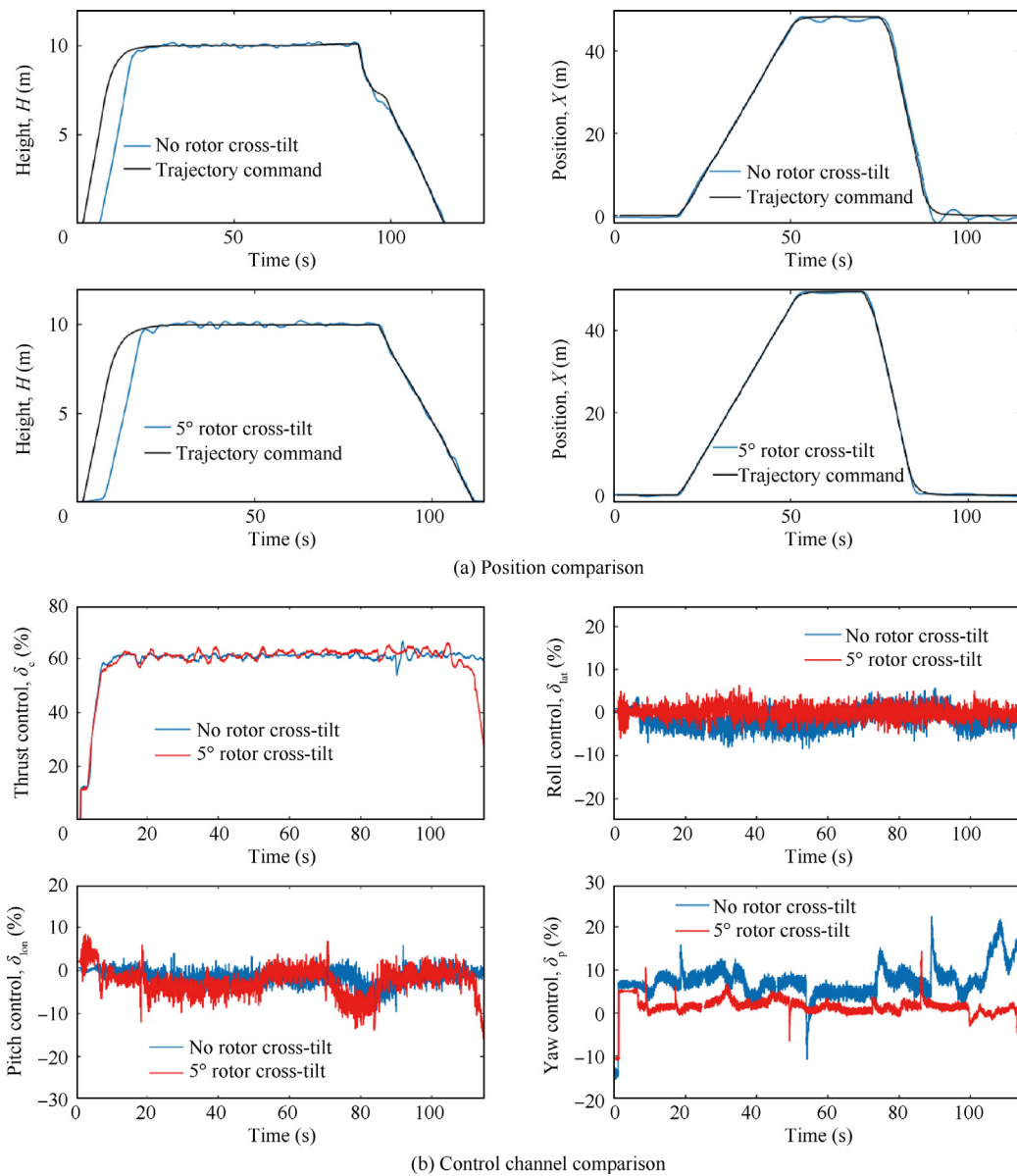
Fig. 23   Comparison of prototype trajectory tracking experiments.

in this paper. Hence, further research is required to evaluate the overall performance enhancement of the manned multi-rotor eVTOL aircraft.

Declaration of competing interest

The authors declare that they have no known competing financial interests or personal relationships that could have appeared to influence the work reported in this paper.

Acknowledgements

References

1. Pavel MD. Understanding the control characteristics of electric vertical take-off and landing (eVTOL) aircraft for urban air mobility. *Aerosp Sci Technol* 2022;**125**:107143.
2. Li C, Qu W, Li Y, et al. Overview on traffic management of urban air mobility(UAM) with eVTOL aircraft. *J Traffic Transp Eng* 2020;**20**(4):35–54.
3. Ploetner KO, Al Haddad C, Antoniou C, et al. Long-term application potential of urban air mobility complementing public transport: An upper Bavaria example. *CEAS Aeronaut J* 2020;**11**(4):991–1007.
4. Reiche C, Goyal R, Cohen A, et al. Urban air mobility market study. Washington, D.C.: NASA Headquarters Aeronautics Research Mission Directorate; 2019. Report No.: HQ-E-DAA-TN65181.
5. de Angelis EL. Stability analysis of a multirotor vehicle hovering condition. *Aerosp Sci Technol* 2018;**72**:248–55.

6. Smeur EJJ, de Croon GCHE, Chu Q. Cascaded incremental nonlinear dynamic inversion for MAV disturbance rejection. *Contr Eng Pract* 2018;**73**:79–90.

7. Gao BK, Liu YJ, Liu L. Fixed-time neural control of a quadrotor UAV with input and attitude constraints. *IEEE/CAA J Autom Sin* 2023;**10**(1):281–3.

8. Lin XB, Liu J, Yu Y, et al. Event-triggered reinforcement learning control for the quadrotor UAV with actuator saturation. *Neurocomputing* 2020;**415**:135–45.

9. Fu CY, Tian YT, Huang HY, et al. Finite-time trajectory tracking control for a 12-rotor unmanned aerial vehicle with input saturation. *ISA Trans* 2018;**81**:52–62.

10. Gai WD, Zhou YC, Zhong MY, et al. Simple adaptive control with an adaptive anti-windup compensator for the unmanned aerial vehicle attitude control. *IEEE Access* 2020;**8**:52323–32.

11. Xu LX, Ma HJ, Guo D, et al. Backstepping sliding-mode and cascade active disturbance rejection control for a quadrotor UAV. *IEEE/ASME Trans Mechatron* 2020;**25**(6):2743–53.

12. Peng C, Cai LH, Qiao GY, et al. Dynamic anti-windup compensation control of yaw movement for a coaxial eight-rotor unmanned flying robot. *2022 4th world symposium on artificial intelligence (WSAI)*; Jilin, China. Piscataway: IEEE; 2022.p. 34–8.

13. Wei HJ, Jiang Y, Luo SX. Adaptive quasi-sliding mode tracking control for quadrotors with input saturation. *2022 41st Chinese control conference (CCC)*; Hefei, China. Piscataway: IEEE; 2022. p. 444–9.

14. Xu QZ, Wang ZS, Zhen ZY. Adaptive neural network finite time control for quadrotor UAV with unknown input saturation. *Nonlinear Dyn* 2019;**98**(3):1973–98.

15. Chen M, Yan K, Wu QX. Multiapproximator-based fault-tolerant tracking control for unmanned autonomous helicopter with input saturation. *IEEE Trans Syst Man Cybern* 2022;**52**(9):5710–22.

16. Nyboe FF, Malle NH, Ebeid E. MPSoC4Drones: An open framework for ROS2, PX4, and FPGA integration. *2022 international conference on unmanned aircraft systems (ICUAS)*; Dubrovnik, Croatia. Piscataway: IEEE; 2022.p.1246–55.

17. Yuan Y, Thomson D, Chen RL. Investigation of lift offset on flight dynamics characteristics for coaxial compound helicopters. *J Aircr* 2019;**56**(6):2210–22.

18. Lee S, Dassonville M. Iterative blade element momentum theory for predicting coaxial rotor performance in hover. *J Am Helicopter Soc* 2020;**65**(4):1–12.

19. Nguyen DH, Liu Y, Mori K. Experimental study for aerodynamic performance of quadrotor helicopter. *Trans Japan Soc Aero S Sci* 2018;**61**(1):29–39.

20. Yu ZM, Yan XF, Chen RL. Prediction of pilot workload in helicopter landing after one engine failure. *Chin J Aeronaut* 2020;**33**(12):3112–24.

21. Chi C, Yan XF, Chen RL, et al. Analysis of low-speed height-velocity diagram of a variable-speed-rotor helicopter in one-engine-failure. *Aerosp Sci Technol* 2019;**91**:310–20.

22. Kennedy G, Fu YC. Topology optimization benchmark problems for assessing the performance of optimization algorithms. *Proceedings of the AIAA scitech 2021 forum*. Reston: AIAA; 2021.